



OPEN

# Classification of impact damage patterns of cement cured soils in Pisha sandstone geopolymer based on critical strain rate

Xiaoze Zhao, Xiaoli Li<sup>✉</sup> & Zhuojun Feng

This study investigates the mechanical properties and damage processes of cement-consolidated soils with Pisha sandstone geopolymer under impact loading using the Hopkinson lever impact test. The mechanical properties of cement-cured soils containing Pisha sandstone geopolymer were examined at various strain rates. The relationship between strain rate and strength of the geopolymer-cemented soil was established. As the strain rate increased, the coefficient of power increase for the Pisha sandstone geopolymer cement-cured soil initially rose before gradually stabilizing. The pore structure of the crushed specimens was analyzed using Mercury intrusion porosimetry. Based on the observed pore changes under impact loading, the pore intervals of the geopolymer-cemented soil were defined. A fitting model linking strain rate and porosity was developed. As strain rate increased, the porosity of the specimens first increased and then decreased, with larger internal pores gradually transforming into smaller ones. The highest porosity was observed at a strain rate of  $64.67 \text{ s}^{-1}$ . Crushing characteristics of the cement-cured soils under impact loading were determined through sieving statistics of the crushed particles. The average particle size of the fragments decreased as the strain rate increased. The fractal dimension initially decreased and then increased with the rise in strain rate, reaching its lowest value at a strain rate of  $64.67 \text{ s}^{-1}$ . Based on the dynamic mechanical properties, microscopic porosity, and fracture characteristics, the critical strain rate and damage form for cement-consolidated soils with Pisha sandstone geopolymer under impact loading were determined. This study offers valuable insights for the practical application of Pisha sandstone geopolymer cement-cured soils in engineering.

**Keywords** Pisha sandstone, Dynamic properties, Strain rate, Crushing characteristics, Pore structure

Pisha sandstone is a loose rock formation widely distributed across the Ordos Plateau in Inner Mongolia, China. Due to the thin overlying layer, low pressure, low degree of rock formation, poor cementation between sand grains, and low structural strength, it may appear to be solid rock. However, it collapses when it rains and disperses in the wind, making it highly susceptible to soil erosion, which causes significant damage to the regional ecosystems<sup>1</sup>. In recent years, many researchers, both domestically and internationally, have made significant contributions to understanding the erosion mechanisms and engineering treatments of Pisha sandstone<sup>2–4</sup>, all of which play a vital role in the region's ecological restoration.

However, Pisha sandstone weathered soil, when mixed with cement, forms a cement-cured soil that exhibits good compressive strength and durability<sup>5</sup>. This material can be used as sub-base material for highway engineering and for hydraulic soil piles in railway roadbeds, offering a new approach to local Pisha sandstone management. Nonetheless, the cement production process generates substantial carbon emissions. In contrast, alkali-activated geopolymers have a simpler preparation process, lower energy consumption, and reduced pollution<sup>6</sup>. Many international studies have explored the use of polymer-consolidated soils in alkali-activated sites<sup>7,8</sup>, highlighting the potential of alkali-activated materials as substitutes for cement. The static properties and microreaction mechanisms of polymer-cement-cured soils in alkali-excited Pisha sandstone have been thoroughly investigated<sup>9</sup>.

Extensive research has been conducted on cement or geopolymer-cured soils. Environmentally hazardous soils have been stabilized by adding additives such as limestone<sup>10</sup>, fly ash<sup>11</sup>, fibers<sup>12</sup>, and soil curing agents<sup>13</sup>, and

College of Water Conservancy and Civil Engineering, Inner Mongolia Agricultural University, Hohhot 010018, China.  
✉ email: sjylxl@imau.edu.cn

the optimal amounts of these curing agents for treating hazardous soils have been determined. The durability of cement-cured soils under freeze-thaw<sup>14</sup> and wet-dry cycles<sup>15</sup> has also been extensively studied, providing substantial technical support for the application of cement-cured soils in engineering projects. However, most current research on the mechanical properties of cement-cured soils focuses primarily on quasi-static mechanics, conducting unconfined compressive strength tests, triaxial tests, and tensile tests.

When cement-cured soils are used as highway subgrade materials, they are often exposed to vibration impact loads from the emergency braking of high-speed vehicles<sup>16</sup>. Similarly, when used in railway foundation piles, these soils are subject to vibration loads caused by heavy trains running at high speeds<sup>17</sup>. A single static compressive strength measure is insufficient for assessing their suitability. Thus, cement-cured soils must possess not only good static properties and durability but, more importantly, strong dynamic properties. Considerable research has been conducted on the impact damage of cementitious brittle materials, with a primary focus on concrete. The dynamic strength of concrete materials typically exhibits strain rate effects<sup>18</sup>, meaning that dynamic strength is strongly correlated with the strain rate. Techniques such as Computed Tomography (CT) and Digital Image Correlation (DIC) have been used to analyze the damage process of concrete under impact loading. It was found that microcracks in concrete damage start at the middle of the rear end of the specimen, then expand continuously along the direction of impact, and finally lead to full damage when the cracks penetrate the material<sup>19</sup>. Most researchers have used numerical simulations to study the damage process of concrete under various impact loads<sup>20,21</sup>. However, concrete is not a homogeneous material due to the inherent randomness of the aggregates, and the mechanical properties and damage processes are significantly influenced by the aggregate effect<sup>22</sup>.

In recent years, significant progress has been made in the study of the damage mechanisms of materials under dynamic loading across various fields. In rock engineering, researchers have explored the energy transfer mechanisms involved in rock fragmentation using finite element modeling, specifically focusing on the energy efficiency and stress distribution of tunnel boring machine (TBM) cutters<sup>23</sup>. Numerical simulations of TBM disk cutters have further clarified the impact of dynamic stress concentration on crack propagation<sup>24</sup>. Additionally, studies on the expansion patterns of preexisting symmetric cracks under blasting loads have provided a theoretical foundation for predicting dynamic fractures<sup>25</sup>. In the realm of material modification, the optimization of plasticity enhancement and compressive strength in fiber-reinforced concrete has demonstrated that microstructural design can significantly enhance the dynamic properties of materials<sup>26</sup>. In contrast, the use of multilayer deformable models in predicting the elasto-plastic behavior of rocks underscores the importance of complex constitutive models for simulating dynamic responses<sup>27</sup>. Notably, research on the shear behavior of soil-concrete interfaces has highlighted the impact of interfacial effects on the material's overall mechanical properties, particularly under dynamic loading, where interfacial slip may aggravate damage<sup>28</sup>. However, most existing studies have concentrated on traditional materials such as rock and concrete. There remains a lack of systematic exploration into the dynamic damage mechanisms of aggregate-free homogeneous materials, such as cement-cured soil, under impact loading. Although the Grady-Kipp model is commonly employed to describe the relationship between fragment size and strain rate<sup>29</sup>, its applicability to cement-cured soils has not been validated.

The core innovation of this study lies in its first-time revelation of the critical strain rate effect in cement-cured soil incorporating Pisha Sandstone geopolymer, as well as the establishment of a multi-scale evaluation system for dynamic damage. Unlike traditional aggregate-based materials, such as concrete, this material exhibits unique strain rate sensitivity due to its homogeneous composition. At the critical strain rate, the damage mode transitions from tensile-dominated to compression-dominated, with the fractal dimension displaying notably small values. Furthermore, by integrating microscopic pore evolution and macroscopic fracture characteristics, this study introduces a dynamic intrinsic model specifically suited for homogeneous materials, providing a theoretical foundation for the impact-resistant design of similar materials. The analysis of pore structure changes post-impact damage delineates pore classification intervals that differentiate it from concrete, and reveals the trends in pore changes under varying strain rates. These findings not only bridge the gap in the study of dynamic mechanics of cured soil materials but also offer a scientific basis for enhancing the durability of ecological restoration projects in Pisha Sandstone regions.

## Materials and methods

### Experimental materials

The Pisha sandstone used in this experiment was sourced from the red Pisha sandstone in the Ordos area, Inner Mongolia Autonomous Region, China. Its physical and mechanical properties are summarized in Table 1. The soil samples were crushed, naturally dried, and then sieved through a 2.36 mm mesh. Jidong brand P.O42.5 ordinary silicate cement was used in the experiment. The metakaolin selected was 1250 mesh highly active metakaolin, a white powder produced by Inner Mongolia Autonomous Region Super Brand Calcined Metakaolin Co.

Natural moisture content/%	Saturated moisture content /%	Permeability coefficient/mm·s <sup>-1</sup>	Porosity/%	Density/g·cm <sup>-3</sup>	Liquid limit/%	Plastic limit/%	Plasticity index
2.7–8.83	18.6–19.5	$5.2 \times 10^{-3}$	31.04–35.15	1.85–1.96	29.30	19.60	9

**Table 1.** Basic physical properties of red Pisha sandstone.

Pisha sandstone quality/%	Cement quality/%	Quality of partial kaolin/%	Water quality /%
71.58	12	3	13.42

**Table 2.** Experimental material ratios.

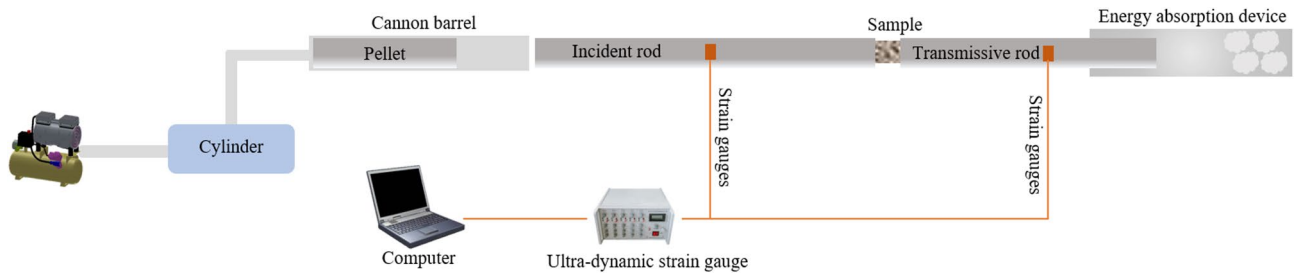


**Fig. 1.** Schematic diagram of the SHPB experimental system.

### Sample preparation and experimental methods

Pisha sandstone geopolymer cement-cured soil specimens were prepared with 12% cement, 3% metakaolin, and liquid sodium silicate as the alkali activator, with a modulus of 1.2. The alkali activator was added to the specimens in a proportion corresponding to an alkali equivalent (expressed as  $\text{Na}_2\text{O}$  mass fraction of the cementitious material) of 2%. A CNC multifunctional electric compactor was used to compact the Pisha sandstone geopolymer cement-cured soils in order to determine their optimum moisture content and maximum dry density. The maximum dry density of the cement-cured soil varied from  $1.857$  to  $1.903 \text{ g}\cdot\text{cm}^{-3}$  based on the percussion test, and a value of  $1.88 \text{ g}\cdot\text{cm}^{-3}$  was chosen for the test. The optimum moisture content ranged from 13.1 to 13.74%, with 13.42% selected for the test. The specific material mix used for the tests is shown in Table 2.

In accordance with the relevant provisions of the Test Procedure for Stabilized Materials of *Inorganic Binding Materials for Highway Engineering* (JTG E51-2009), the test materials were sequentially loaded into the mixer for thorough mixing. The mixed materials were then placed into steel molds and pressed to form  $\varnothing 50 \text{ mm} \times \text{H}50 \text{ mm}$  specimens. These specimens were subjected to alkali activation in a high and low-temperature alternating humidity and heat test chamber, where they were treated at  $80 \text{ }^\circ\text{C}$  for 12 h. After this process, the specimens were transferred to a standard curing box and maintained for 60 days before testing.

### Experimental equipment and principles

An experimental system with a Separate Hopkinson Pressure Bar (SHPB) of  $\varnothing 80 \text{ mm}$  was selected for the impact test, as shown in Fig. 1. The system primarily consists of a launching device, an incident bar, a transmitting bar, an absorbing device, and a data acquisition system. The bullet, incident bar, and transmitting bar are steel rods with a diameter of  $\varnothing 80 \text{ mm}$ , and lengths of 0.5 m, 3.5 m, and 2.4 m, respectively. These rods have a Young's modulus ( $E_s$ ) of 210 GPa and a density of  $7800 \text{ kg}/\text{m}^3$ . The data acquisition system utilizes the LCS-1D dynamic resistance strain gauge, produced by Qinquangdao Langzhen Electronic Technology Co. Ltd, with a sampling frequency of 2 MHz and a sampling length of 10 K.

During the impact process, the bullet strikes the incident rod at a certain speed, generating an incident wave. When the incident wave reaches the end of the test block, part of the wave is reflected back, forming the reflected wave, due to the difference in wave impedance. The remaining portion of the wave passes through the test block, forming the transmitted wave, which is ultimately absorbed by the absorption device. Sensitive strain gauges attached to the incident and transmitting rods detect the changes in weak voltage signals. The signal is then amplified using the ultra-dynamic resistance strain gauge to obtain the waveforms under impact. Finally, the voltage signal is converted into a strain signal using Eq. (1):

$$\mu_\varepsilon = \frac{4U_a(V) \times 10^{-6}}{K_1 U_b(V) n K_2} \quad (1)$$

Where  $\mu_\varepsilon$  represents microstrain.  $U_a$  is the voltage signal measured during the test in V.  $K_1$  is the sensitivity coefficient of the strain gauge, and the test was conducted with BE120-3AA type resistance strain gauge manufactured by China Aviation Industry Electro-Mechanical Instrument Company Limited, and the sensitivity coefficient was 2.22.  $U_b$  represents the bridge box voltage, 2.0 V.  $n$  is the number of bridge arms, the test adopts the working principle of pair-arm bridge, so the number of bridge arms is 2.  $K_2$  is the amplification factor of the strain gauge, and the amplification factor of the LCS-1D dynamic resistance strain gauge used in this experiment is 2.0.

According to the theory of one-dimensional stress wave and stress uniformity assumption<sup>30</sup>, The measured incident wave  $\varepsilon_i$ , reflected wave  $\varepsilon_r$  and transmitted wave  $\varepsilon_t$  can be used to calculate the strain rate  $\dot{\varepsilon}(t)$ , strain  $\varepsilon(t)$  and stress  $\sigma(t)$  of the specimen material:

$$\begin{aligned}\dot{\varepsilon}(t) &= -\frac{2C_e}{L_s}\varepsilon_r(t) \\ \varepsilon(t) &= -\frac{2C_e}{L_s}\int_0^t \varepsilon_r(t')dt' \\ \sigma(t) &= \frac{A_e}{A_s}E_e\varepsilon_t(t)\end{aligned}\quad (2)$$

Where  $A_s$  and  $L_s$  are the cross-sectional area and length of the specimen.  $A_e$ ,  $E_e$  and  $C_e$  are the cross-sectional area, modulus of elasticity and longitudinal wave velocity of the incident or transmitted rod, respectively.

In the SHPB test, there is no universally standardized specimen size; however, the specimen size significantly influences the inertia effect during impact and the friction effect on the end face of the guide rod, which in turn affects the accuracy of the test results. It is recommended that the specimen's length-to-diameter ( $L/D$ ) ratio should range from 0.5 to 1.0, with the specimen diameter being approximately 80% of the rod diameter<sup>31</sup>. In accordance with the relevant provisions of the Test Procedure for *Inorganic Binding Material Stabilization in Highway Engineering* (JTG E51-2009), the test block size was determined to be  $\varnothing 50\text{mm} \times 50\text{mm}$ . Before the test, the surface of the test block was polished with sandpaper to ensure it was sufficiently smooth. Vernier calipers were used to measure the size of the test block, with the error required to be within 0.01 mm before proceeding with the test.

The microporosity test was conducted using the AutoPore IV 9500 fully automatic Mercury intrusion porosimeter, produced by MICROMERITICS, USA.

## Test results and analysis of dynamic mechanical properties

### Stress-strain

Impact tests were conducted on Pisha sandstone geopolymers cement-cured soil specimens at air pressures ranging from 0.04 to 0.3 MPa. Based on the strain-time relationship of the reflected signals under different impact air pressures, the strain rate variation of the specimens was calculated using Eq. (2), as shown in Fig. 2. As observed in the figure, with increasing impact air pressure, the strain rate of the Pisha sandstone geopolymers cement-cured soil specimens continuously rises. Under impact air pressures ranging from 0.04 to 0.3 MPa, the strain rate of the specimens varied between approximately 30 and 170  $\text{s}^{-1}$ , demonstrating a high rate of change in strain. The strain rate under these conditions reached up to a thousand times that of traditional microcomputer servo presses. As the impact air pressure increased further, the rate of strain rate growth gradually decreased. A quadratic relationship between impact air pressure and the strain rate of the specimens was fitted, showing a high degree of correlation.

Using the strain signals measured by each rod and applying Eq. (2), the stress-strain relationship of the Pisha sandstone geopolymers cement-cured soil specimens under different strain rates can be obtained, as shown in Fig. 3. The Pisha sandstone geopolymers cement-cured soil specimens exhibited brittle damage characteristics under impact, and their stress-strain curves displayed clear patterns with increasing impact air pressure. This indicates that the specimens exhibit a significant strain rate effect in dynamic damage. During the initial impact stage, as the stress wave energy increased, the stress-strain curve of the specimen rose rapidly and reached peak stress in a short period, with the material remaining in the linear elastic phase. A notable correlation was observed between the peak stress and strain rate at various strain rates. The peak stress increased continuously with rising strain rates and tended to stabilize once the strain rate exceeded 170  $\text{s}^{-1}$ .

### Dynamic response analysis

The Dynamic Increase Factor (*DIF*) is the ratio of the dynamic strength of a material to its static strength, serving as a key parameter to describe the dynamic properties of cement-cured soils. It is typically correlated with the material's strain rate. Numerous studies have shown that the power increase coefficient of brittle materials is usually non-linearly related to the logarithm of the strain rate<sup>32,33</sup>. To investigate the dynamic response of Pisha sandstone geopolymers cement-cured soil specimens under high-velocity impact, the test data were organized as shown in Table 3. The relationship between the power increase coefficient and the strain rate of the cement-cured soil specimens with Pisha sandstone geopolymers is depicted in Fig. 4, where the data were fitted to segments. The dynamic response relationship of the cement-cured soil with Pisha sandstone geopolymers is expressed by Eq. (3).

Pisha Sandstone geopolymers cement-cured soils exhibit higher strain rate sensitivity and dynamic strength growth compared to conventional cement-stabilized soils. The *DIF* of Pisha Sandstone geopolymers cement-stabilized soil is significantly higher than that of conventional cement-stabilized soil at high strain rates ( $> 64.67\text{ s}^{-1}$ ). For instance, at a strain rate of 169.31  $\text{s}^{-1}$ , its *DIF* reaches 2.14, while the *DIF* of conventional hydraulic clay is typically lower due to its higher plasticity. For example, the *DIF* of graphene oxide-doped hydraulic clay is less than 1.4<sup>34</sup>, and the *DIF* of in-situ cemented backfill ranges from 1.02 to 1.74<sup>35</sup>.

Based on the peak stress magnitude under impact loading of the Pisha sandstone geopolymers cement-cured soil specimens, the coefficient of power increase was analyzed in two stages. In the first stage, where the strain rate is less than 64.67  $\text{s}^{-1}$ , as the strain rate of the specimen increases during the impact damage process, the coefficient of power increase rises. This coefficient exhibits a linear relationship with the logarithm of the strain rate. In the second stage, where the strain rate ranges from 64.67  $\text{s}^{-1}$  to 160  $\text{s}^{-1}$ , the *DIF* increases from 1.0 to 2.1. During this stage, the Pisha sandstone geopolymers cement-cured soil specimens undergo a large range of strain rate increases, and their *DIF* increases as well, with the coefficient of power increase correlating non-linearly with the logarithm of the strain rate.

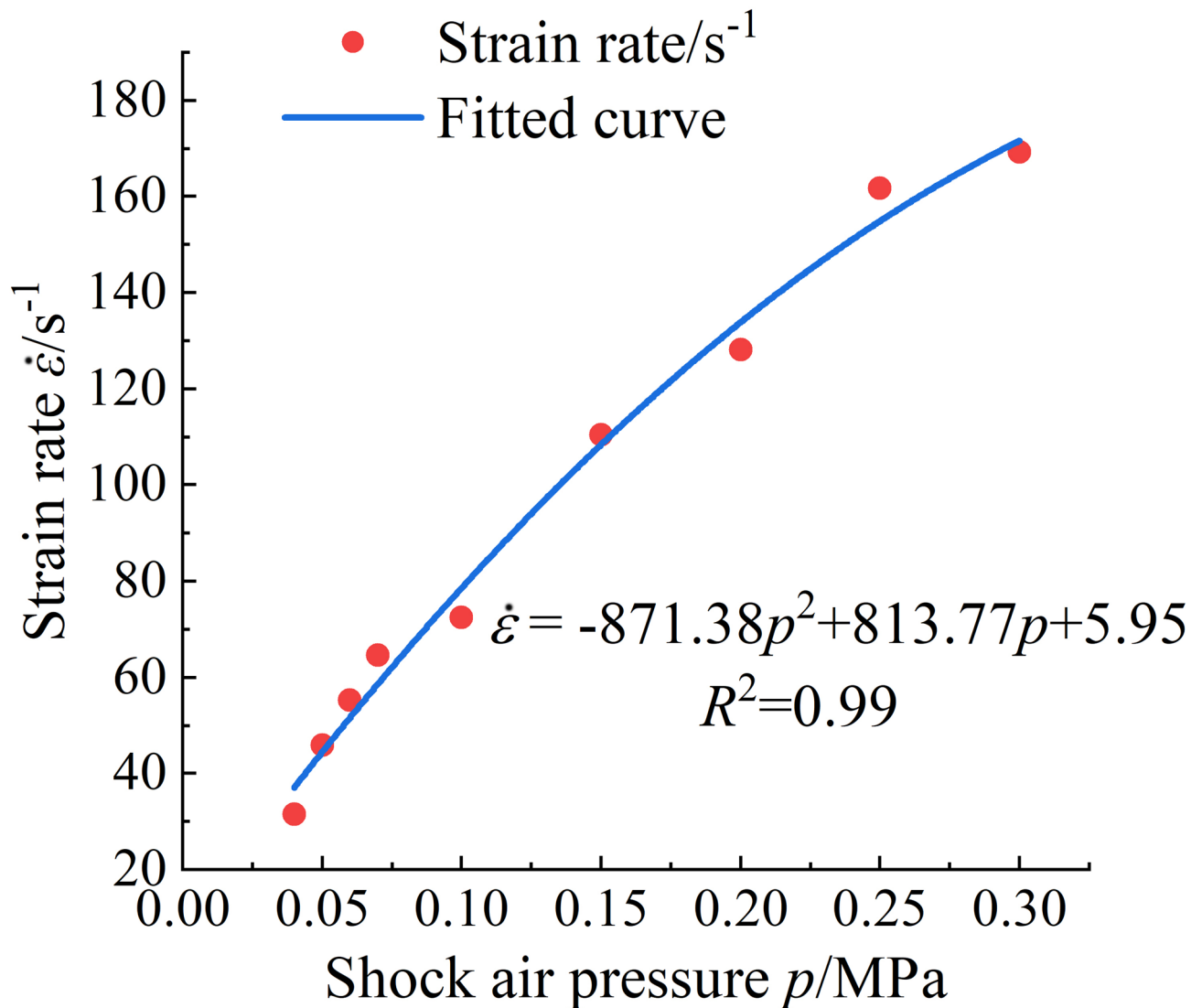


Fig. 2. Strain rate-impact air pressure relationship for test blocks under impact loading.

$$DIF = \begin{cases} 1.7 \lg \dot{\epsilon} - 1.95 & \dot{\epsilon} \leq 64.67 \text{ s}^{-1} \\ -1.77 (\lg \dot{\epsilon})^2 + 9.62 \lg \dot{\epsilon} - 10.39 & 64.67 \text{ s}^{-1} \leq \dot{\epsilon} \leq 160 \text{ s}^{-1} \end{cases} \quad (3)$$

### Analysis of the damage process based on microscopic pore changes Analysis of microscopic pore structure under dynamic loading

To further investigate the characteristics of cement-cured soil with Pisha sandstone geopolymer under impact damage, microporosity analysis of the crushed specimens was performed using Mercury intrusion porosimetry. The changes in porosity and average pore diameter of the specimens under different strain rates are shown in Fig. 5. As the strain rate increases, the porosity of the crushed specimens first increases and then decreases; however, it remains higher than the porosity of the undamaged specimens. The maximum porosity of 28.3% was observed at a strain rate of  $64.67 \text{ s}^{-1}$ , representing a 2.67% increase compared to the undamaged specimen. Similarly, the average pore size of the crushed specimens first increases and then decreases with increasing strain rate, but it remains larger than the average pore size of the undamaged specimens. The maximum average pore size of 76.9 nm was reached at a strain rate of  $64.67 \text{ s}^{-1}$ , which is an increase of 15.1 nm compared to the undamaged specimen.

The differential distribution curves of the pore structure of the specimens under damage at different strain rates are shown in Fig. 6. As observed in the figure, the differential distribution curves of the Pisha sandstone geopolymer cement-cured soil specimens primarily exhibit two peaks, corresponding to pore diameters in the ranges of 10–100 nm and 1500–15,000 nm, respectively. The pore diameter at the peak point of the differential curve represents the most prevalent pore size, i.e., the pore size with the highest probability of occurrence. In the 10–100 nm pore size range, as the strain rate increases, the peak point shifts to the left. The highest peak occurs in the undamaged specimen, while the lowest peak and smallest peak area are observed at a strain rate

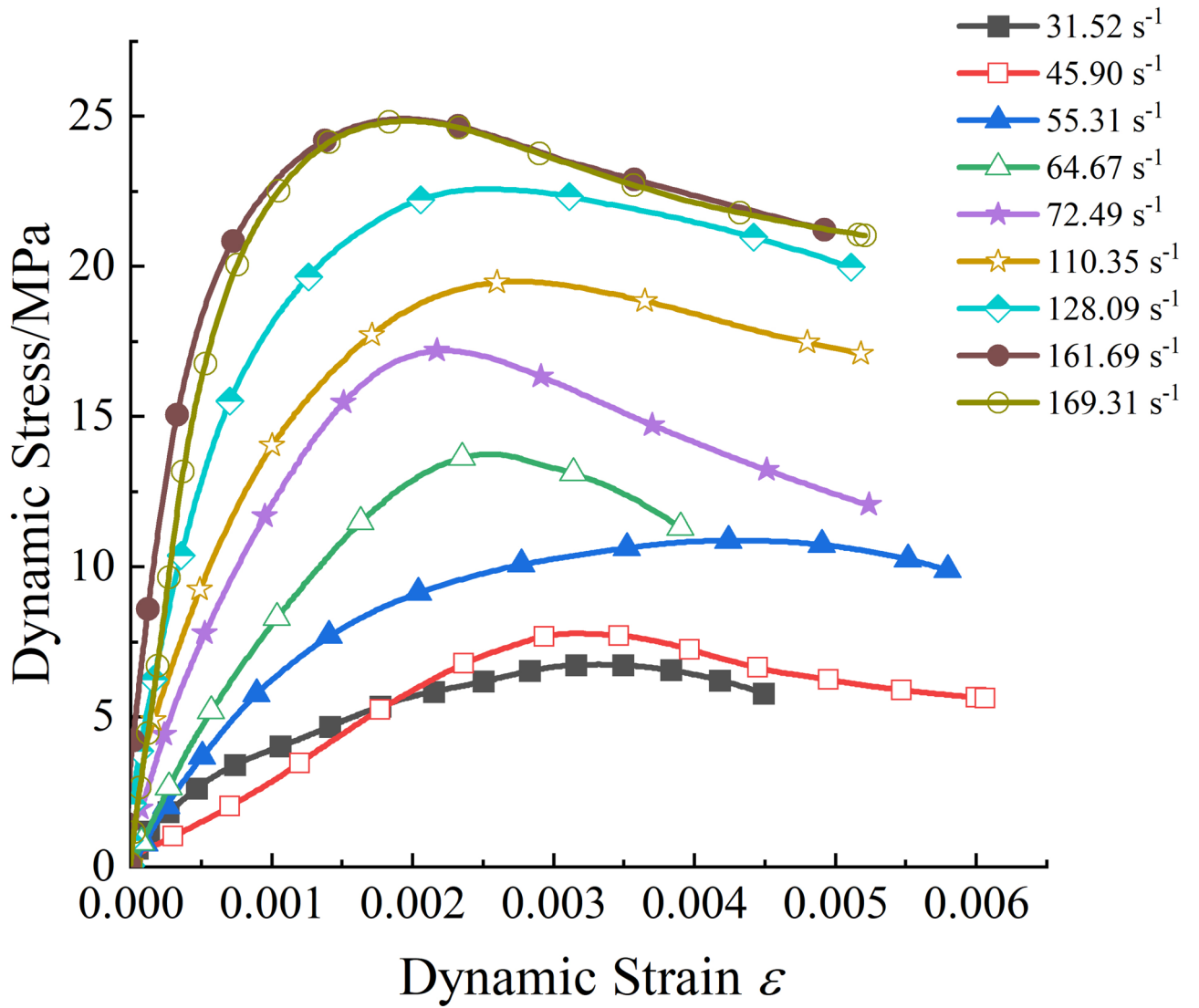


**Fig. 3.** Stress-strain curves of Pisha sandstone geopolymer cement cured soil specimens at different strain rates.

Strain rate $\dot{\epsilon}$	$\lg \dot{\epsilon}$	Static strength/MPa	Dynamic strength/MPa	DIF
31.52	1.50	11.82	7.50	0.63
45.90	1.66	11.82	10.21	0.86
55.31	1.74	11.82	12.21	1.03
64.67	1.81	11.82	13.74	1.16
72.49	1.86	11.82	17.23	1.46
110.35	2.04	11.82	19.85	1.68
128.09	2.11	11.82	22.73	1.92
161.69	2.21	11.82	25.28	2.14
169.31	2.22	11.82	24.97	2.11

**Table 3.** Strain rate and dynamic strength of Pisha sandstone geopolymer hydromulch test blocks under different impact loads.

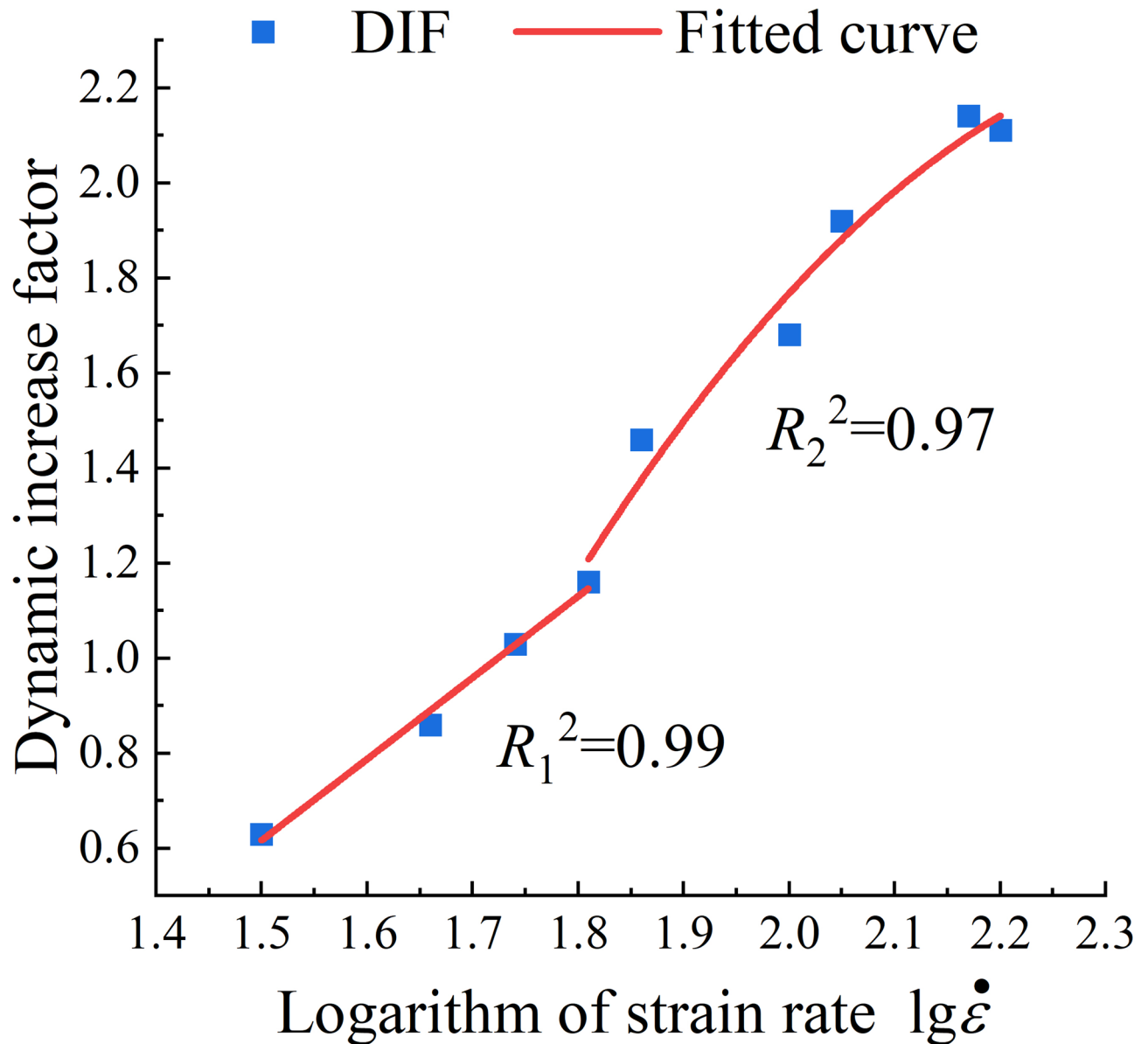


**Fig. 4.** Logarithmic relationship between dynamic increase coefficient and strain rate of Pisha sandstone ground aggregate cement cured soil specimens.

of  $64.67 \text{ s}^{-1}$ . This indicates that impact loading reduces the porosity in this pore size interval, with the lowest porosity observed at a strain rate of  $64.67 \text{ s}^{-1}$ . In the 1500–15,000 nm pore size range, the peak point increases and then decreases with increasing strain rate, with the lowest peak observed in the undamaged specimen.

The extreme point of porosity occurs at a strain rate of  $64.67 \text{ s}^{-1}$ , and the power increase coefficient of the cement-cured soil in Pisha sandstone geopolymer also exhibits a cutoff point at this strain rate. Based on the above observations, the specimen under the  $64.67 \text{ s}^{-1}$  strain rate condition can be considered as the pore characteristic cutoff point. The porosity of the damaged specimen can be modeled by fitting the porosity to the strain rate, with the resulting model shown in Eq. (4):

$$\eta = \begin{cases} 0.0887e^{\dot{\epsilon}/18.10} + 25.15 & \dot{\epsilon} \leq 64.67 \text{ s}^{-1} \\ 27.29 \times (\dot{\epsilon} - 64.67)^{-0.0042} & \dot{\epsilon} \geq 64.67 \text{ s}^{-1} \end{cases} \quad (4)$$

where  $\eta$  is the porosity and  $\dot{\epsilon}$  is the strain rate. The fitted relationship between the strain rate of the specimen and the porosity after crushing is shown in Fig. 7. From the figure, it is evident that the porosity of the specimen is highly correlated with the strain rate, and the model fit is strong, effectively capturing the relationship between the two.

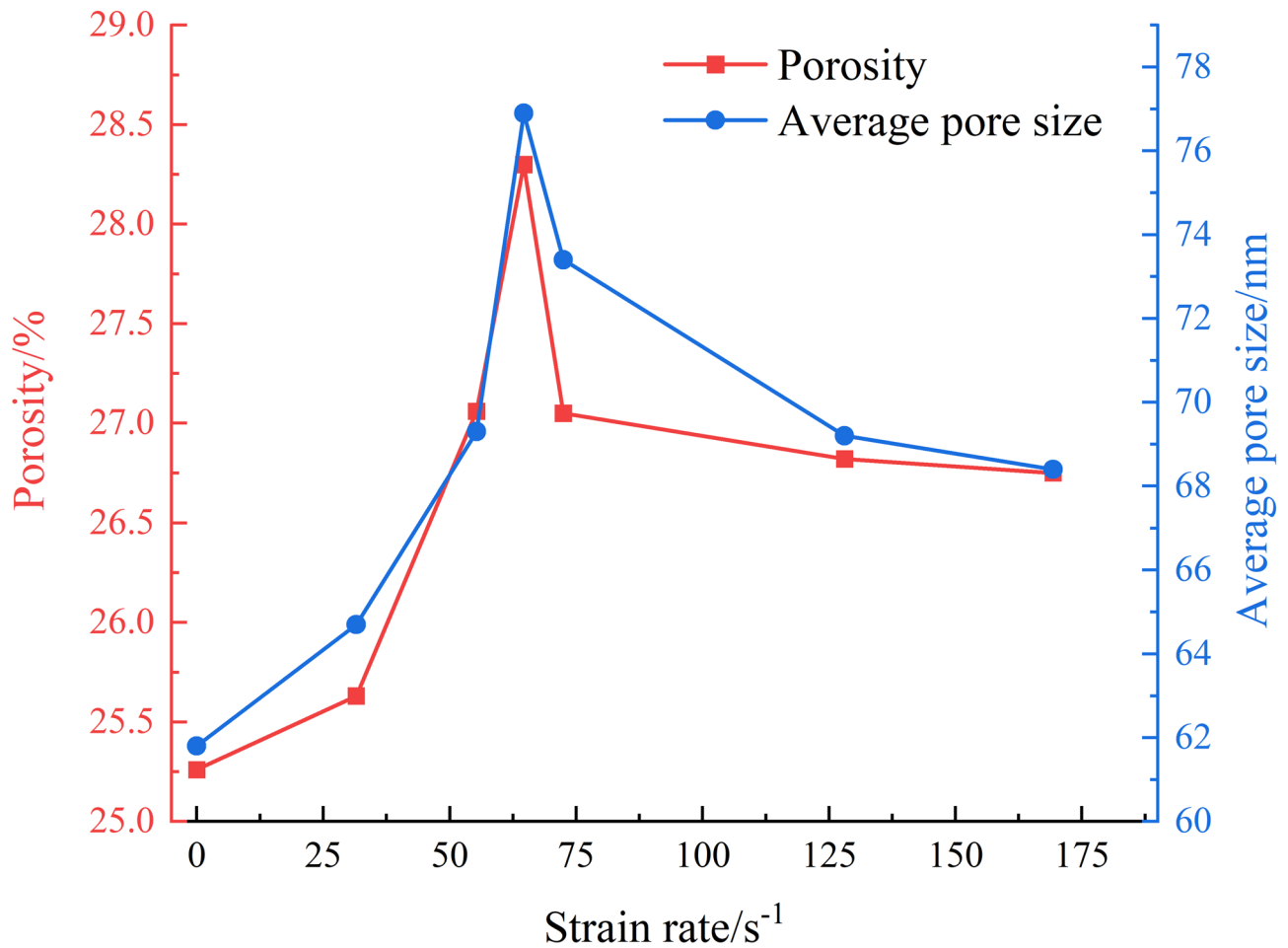


**Fig. 5.** Relationship between porosity and average pore size variation of specimens under different strain rate damage.

### Pore structure classification

The change in the volume of each pore size in the test block under different loads, compared to the volume of each pore size in the test block that was not subjected to load, is shown in Fig. 8. The difference in the vertical coordinates in the graph reflects the trend of the pore structure under different loads. Positive vertical coordinates represent an increase in pore volume share, while negative values indicate a decrease. Based on the intersection of the volume change of each pore size with the  $y=0$  axis in the figure, the pore sizes can be roughly classified into several intervals: micropores ( $< 10$  nm), small pores (10–150 nm), medium pores (150–15000 nm), and large pores ( $> 15000$  nm). In the  $< 10$  nm pore size interval, the volume change of each pore size under different loads is minimal, indicating that impact loading has a small effect on the pore structure in this range. In the 10–150 nm pore size interval, the volume of each pore size under different loads is smaller than the volume of the unloaded specimen, indicating that impact loading causes compression of the pores in this range. In the 150–15,000 nm pore size interval, which exhibits the most significant change in pore size under loading conditions, the volume of each pore size under load is greater than that of the unloaded specimen, indicating that impact loading leads to the expansion and stretching of pore spaces in this range. In the  $> 15,000$  nm pore size interval, impact loading has less of a compressive effect on pore volume and primarily induces expansion and stretching of the large pores.

Based on the classification method described above, the pores in the specimen were divided into four categories: micropores ( $< 10$  nm), small pores (10–150 nm), medium pores (150–15000 nm), and large pores ( $> 15000$  nm). The distribution of the pore structure of the cement-cured soil with Pisha sandstone geopolymer under different strain rate damage conditions is shown in Table 4.

As shown in Table 4, the porosity of the Pisha sandstone geopolymer cement-cured soil specimens increased after impact crushing compared to before the damage. This indicates that the specimens absorbed a significant amount of energy during the impact, which caused the volume to compress and then expand, resulting in an increase in the pore space between soil particles. As the strain rate of the Pisha sandstone geopolymer cement-consolidated soil increases during impact damage, the porosity after crushing shows a tendency to first increase and then decrease.

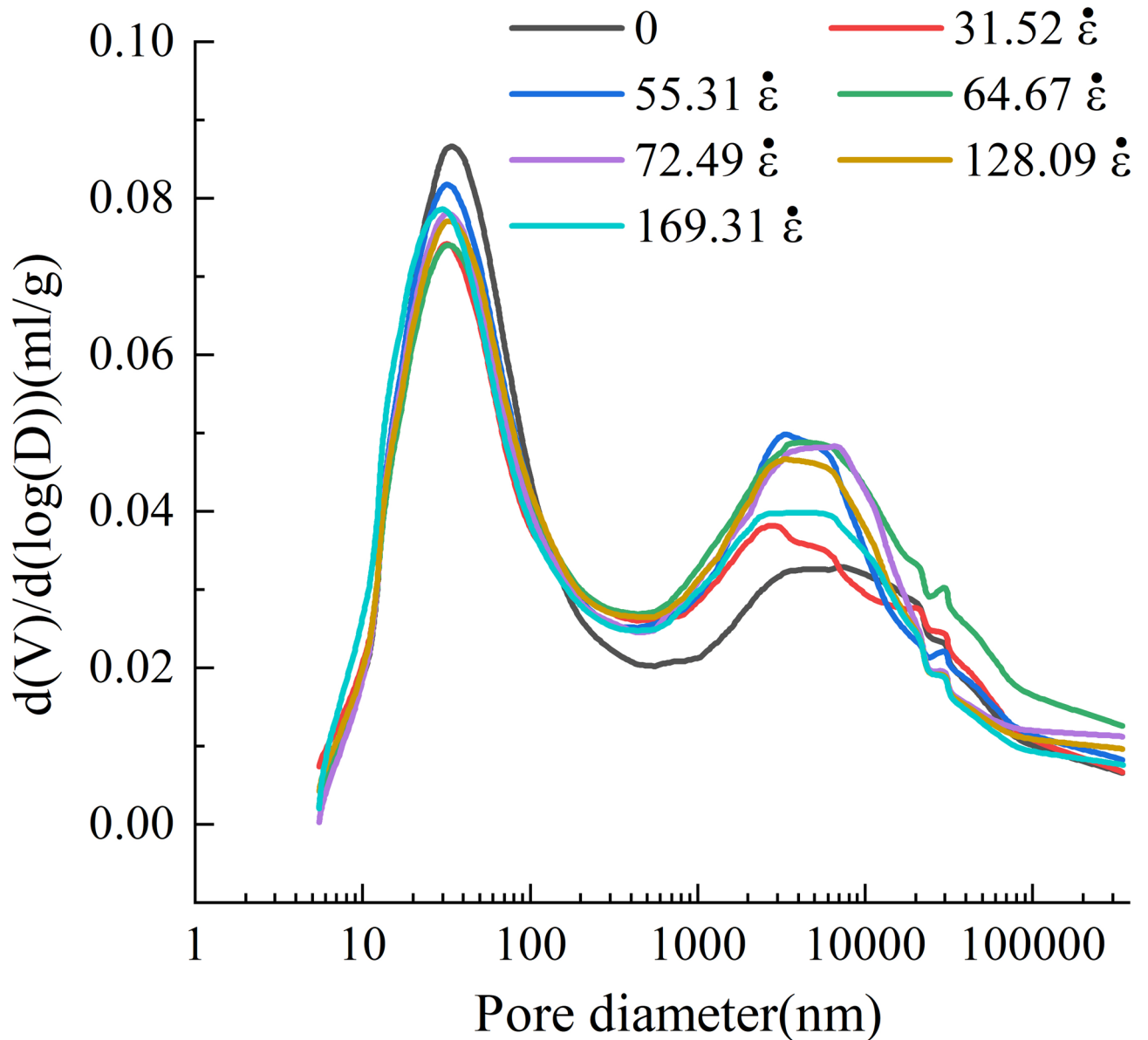


**Fig. 6.** Differential distribution curves of pore structure of specimens damaged by different strain rates.

The percentage of pores in the micropore (<10 nm) interval varies minimally with increasing strain rate. The percentage of pores in the small pore (10–150 nm) interval initially decreases and then increases, reaching a minimum at a strain rate of  $64.67 \text{ s}^{-1}$ . The percentage of pores in the mesopore (150–15000 nm) interval continues to increase with the increasing strain rate. The percentage of pores in the macropore (>15000 nm) interval increases and then decreases, reaching a maximum at a strain rate of  $64.67 \text{ s}^{-1}$ .

A strain rate of  $64.67 \text{ s}^{-1}$  was identified as a critical value for pore alteration in cement-cured soils of Pisha sandstone. When the strain rate is less than  $64.67 \text{ s}^{-1}$ , impact damage to the specimen is primarily dominated by shear damage after compression. The specimen then expands, generating tension, which results in an increase in internal porosity, a decrease in the proportion of small pores (10–150 nm), and an increase in the proportion of large pores (>15000 nm). When the strain rate exceeds  $64.67 \text{ s}^{-1}$ , the impact force increases, and the specimen undergoes compression damage, leading to an increase in overall compactness through extrusion. As a result, some of the large pores are transformed into small pores, causing the percentage of small pores (10–150 nm) to increase and the percentage of large pores (>15000 nm) to decrease.

## Analysis of damage processes based on changes in crushing patterns

### Crushing pattern and crushing characteristics

The crushing pattern of Pisha sandstone geopolymer cement-cured soil under different impact loads is shown in Fig. 9. As observed in the figure, at a strain rate of  $31.52 \text{ s}^{-1}$ , the specimen exhibits only partial spalling, with the overall structure remaining intact. At a strain rate of  $55.31 \text{ s}^{-1}$ , all sides of the specimen are fractured, and

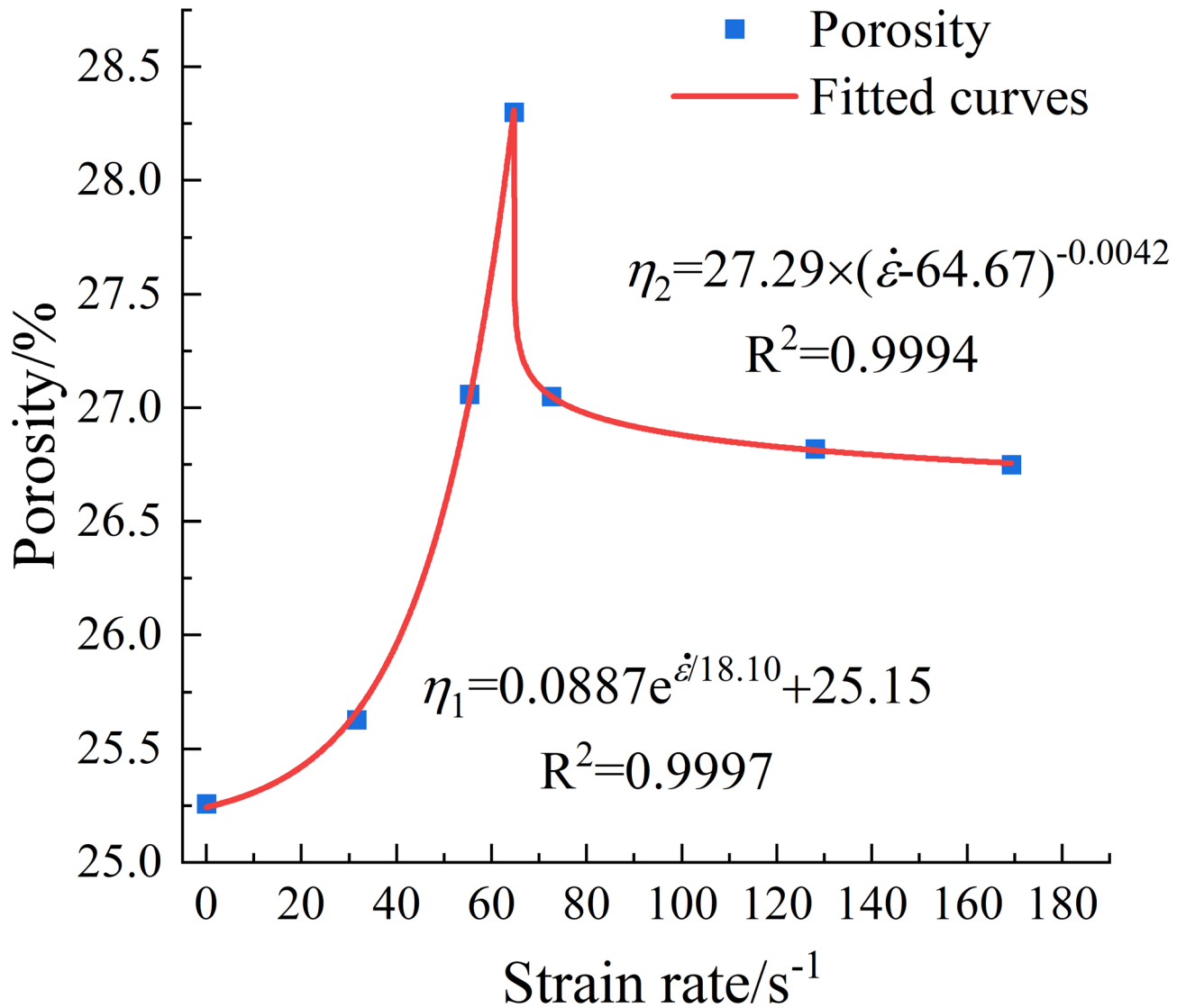


**Fig. 7.** Relationship between strain rate and porosity of Pisha sandstone ground aggregate cement cured soil specimens.

the crushed block predominantly exhibits a flaky shape. When the strain rate exceeds  $64.67 \text{ s}^{-1}$ , the structure of the test block is completely destroyed, and the crushed block predominantly takes on a block shape. As the strain rate increases, the diameter of the crushed block decreases.

The crushed soil samples were sieved using a standard square-hole sieve with mesh sizes ranging from 0.63 to 26.5 mm. The mass of each portion of the crushed pieces was weighed to obtain the distribution of particle sizes for the Pisha sandstone geopolymer cement-cured soil test blocks. Weighted calculations based on the mass share of blocks with different particle sizes were used to determine the average block size of the fragments at different levels of damage. Mass fractal modeling, based on the particle size distribution of rock fragments<sup>36</sup>, was employed to establish the mass-size relationship. This relationship can be used to calculate the fractal dimension  $D$  of the particle size distribution of the fragments, which is expressed as:

$$\lg [M(x)/M_z] = (3 - D) \lg d_x \quad (5)$$

Where  $M(x)$  and  $M_z$  denote the total mass under the sieve of a certain particle size and the total mass of fragments, respectively, in g.  $d_x$  is the standard sieve size in mm.  $D$  is the fractal dimension. With  $\lg d_x$  as the horizontal coordinate and  $\lg [M(x)/M_z]$  as the vertical coordinate. The fractal dimension of the Pisha sandstone geopolymer cement-cured soil specimens can be determined from the slope of the fitted straight line. The crushed grain sizes of the Pisha sandstone geopolymer cement-cured soil specimens at different strain rates are presented in Table 5. As the strain rate increases, the degree of fragmentation of the Pisha sandstone geopolymer cement-cured soil test blocks shows a trend of decreasing mass of large-diameter blocks and an increasing number of small-diameter blocks, resulting in a gradual increase in the overall fragmentation of the test blocks.

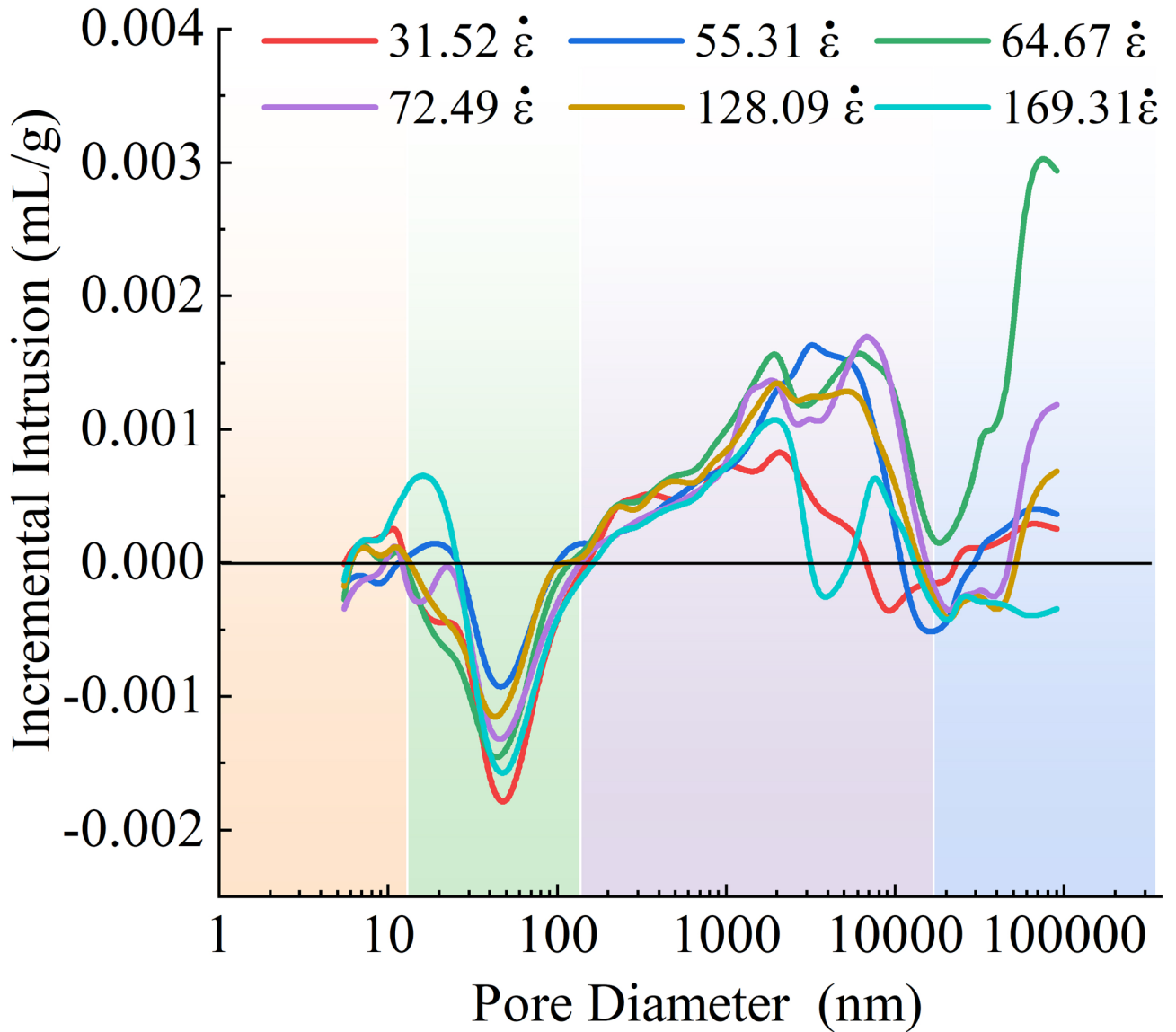
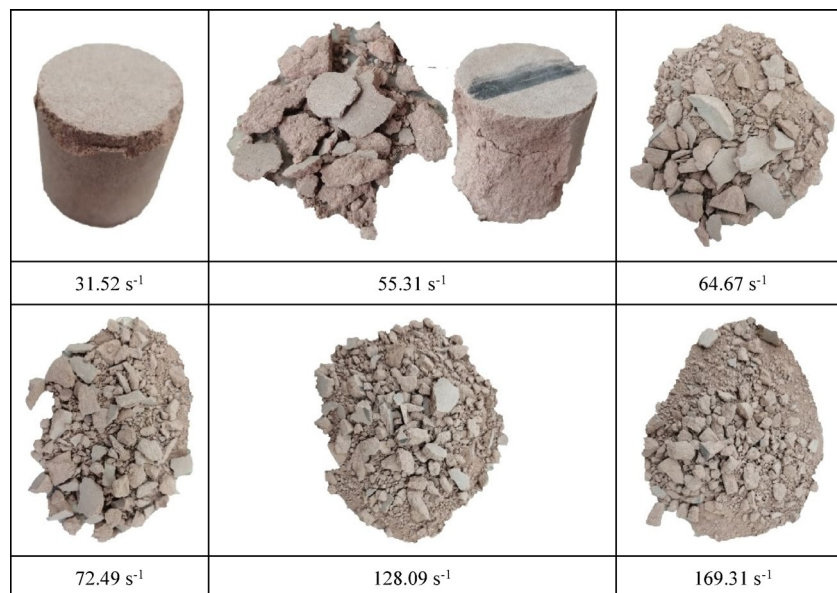


Fig. 8. Volume change of each aperture of test blocks under different strain rates.

Strain rate/s <sup>-1</sup>	Porosity/%	Pore volume fraction /%			
		< 10 nm	10–150 nm	150–15,000 nm	> 15,000 nm
0	25.26	2.20	44.87	35.45	17.48
31.52	25.63	2.53	39.17	40.41	17.89
55.31	27.06	1.78	40.02	41.86	16.34
64.67	28.30	1.98	34.60	41.71	21.71
72.49	27.05	1.67	37.82	43.36	17.15
128.09	26.82	1.66	38.60	43.07	16.17
169.31	26.75	1.71	40.16	42.65	15.48

Table 4. Pore structure of Pisha sandstone geopolymer cement cured soil under different strain rate damage.

From the table, it can be seen that as the strain rate increases, the fractal dimension of the crushed blocks of Pisha sandstone geopolymer cement-cured soil specimens first decreases and then increases, reaching the lowest value at a strain rate of 64.67 s<sup>-1</sup>, after which it gradually increases. This behavior can be attributed to the fact that at low strain rates, the diameter of the fragmented blocks is mainly concentrated in the large block size range. As the strain rate increases, the degree of specimen fragmentation sharply increases, causing the fragmented block



**Fig. 9.** Crushing pattern of test blocks under different impact loads.

Strain rate/s <sup>-1</sup>	Average block size/mm	Fractal dimension	Percentage of block mass in a certain particle size interval(%)						
			> 26.5 mm	10–26.5 mm	5–10 mm	2.5–5 mm	1.25–2.5 mm	0.63–1.25 mm	< 0.63 mm
45.90	36.34	2.5416	94.49	0	1.55	1.48	0.70	0.51	1.40
55.31	22.91	2.5401	41.07	34.79	7.33	5.66	2.62	2.16	5.72
64.67	13.57	2.4329	7.64	50.28	13.03	9.30	4.14	4.04	10.40
72.49	8.69	2.5982	0	37.29	15.48	12.78	5.98	6.22	22.12
110.35	6.85	2.6123	0	23.79	22.68	13.99	7.52	7.24	24.54
128.09	6.80	2.6497	0	24.17	21.94	11.84	7.45	7.68	27.72
169.31	5.46	2.6543	0	14.77	25.18	14.37	8.75	9.59	27.61

**Table 5.** Crushed block size statistics of Pisha sandstone ground aggregate cement cured soil specimens under impact loading.

diameter to shift towards smaller sizes. At a strain rate of  $64.67 \text{ s}^{-1}$ , the crushed grain sizes of the specimen are more evenly distributed, resulting in the smallest fractal dimension. For high strain rates, the Pisha sandstone geopolymer cement-cured soils converge to a final fractal dimension of 2.65. The mean block diameter of the specimens gradually decreased with increasing strain rate, from 36.34 mm to 5.46 mm.

### Relationship between strain rate and macroscopic fragmentation

Quasi-static compression damage typically results in the Pisha sandstone geopolymer cement-cured soil specimens breaking at an oblique angle of  $45^\circ$  into two parts<sup>5</sup>. However, dynamic fracture causes the specimens to break into several smaller pieces after undergoing continuous fracture. The compression damage process of the test block under impact loading can be divided into three stages: splitting, expansion, and tensile fracture. Under impact loading, cracks form rapidly on the outer surface of the test block, causing it to expand under compression. Tensile fracture occurs in the block between different cracks. The higher the impact air pressure, the more micro-cracks are generated inside the block due to unloading obstruction, and crack bifurcation leads to a greater degree of fragmentation<sup>37</sup>.

The crushing theory, first proposed by Mott and later improved by Grady and Kipp, suggests that the average fragment size of the crushed material follows a power function of the strain rate<sup>29</sup>. The relationship between the strain rate and degree of fragmentation of the Pisha sandstone geopolymer cement-cured soil specimens is shown in Fig. 10. As seen in the figure, with increasing strain rate, the degree of fragmentation of the specimen gradually increases, and the average block diameter rapidly decreases. The average block size, obtained through function fitting, shows a power function relationship with the strain rate, with a high fit, consistent with the Grady-Kipp model. As the strain rate increases, the fractal dimension of the specimen first decreases and then increases, reaching its lowest value at a strain rate of  $64.67 \text{ s}^{-1}$ . This indicates that fragmentation is most heterogeneous under this strain rate. When the strain rate exceeds  $64.67 \text{ s}^{-1}$ , the fractal dimension of the Pisha sandstone geopolymer cement-cured soil specimens follows a power function relationship with the strain rate.

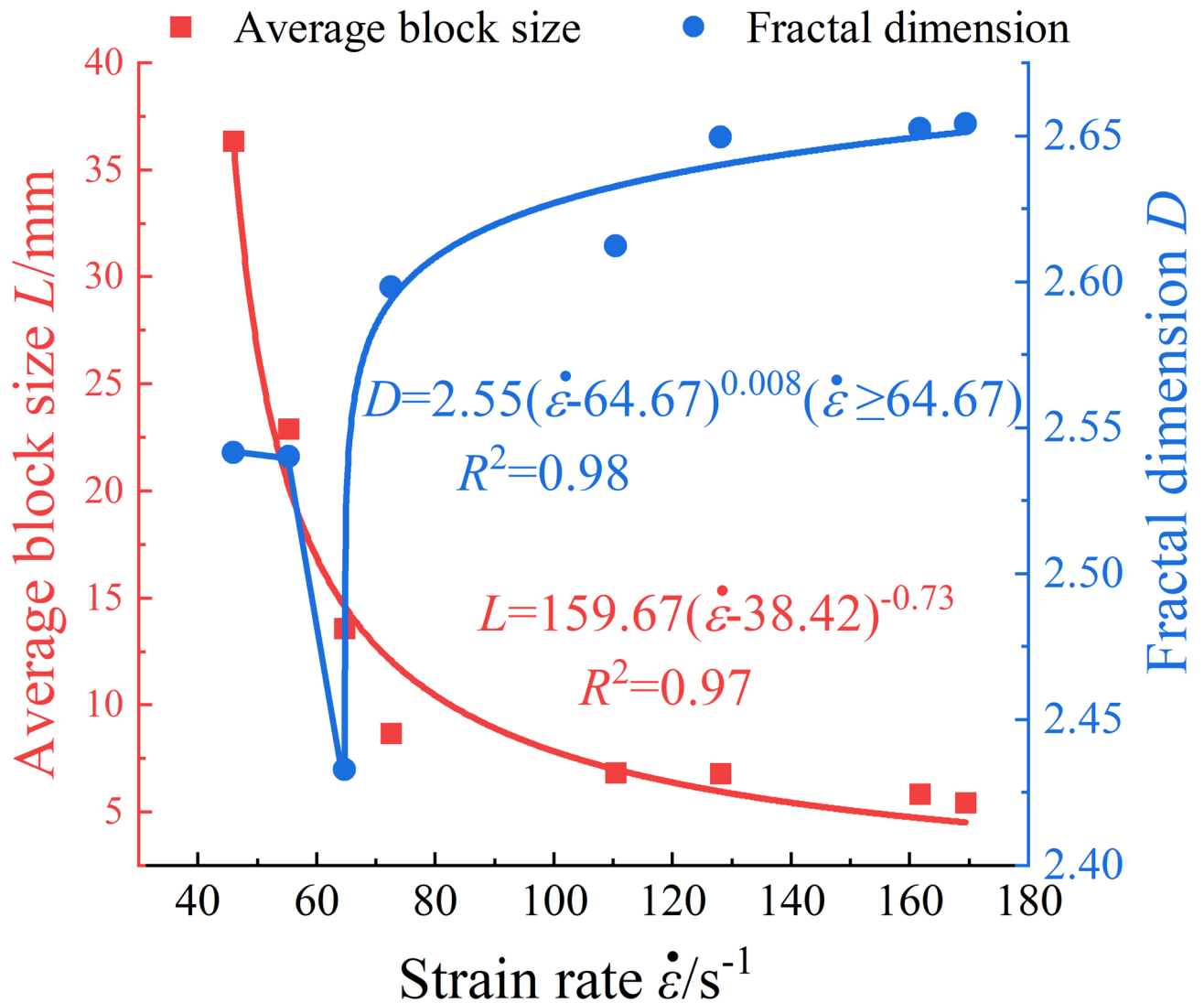


**Fig. 10.** Crushing degree—strain rate relationship of Pisha sandstone ground aggregate cement cured soil specimens.

Crushing fractal analysis provides a better understanding of the macroscopic crushing characteristics of Pisha sandstone geopolymer cement-cured soil under dynamic loading, while porosity is a crucial feature of the specimen's microstructure after impact crushing. Both the fractal dimension and microporosity of the cement-cured soil with Pisha sandstone geopolymer under dynamic loading reached their peak at a strain rate of  $64.67 s^{-1}$ , which was thus taken as the cutoff point.

When the strain rate is less than  $64.67 s^{-1}$ , as the strain rate increases, the specimen experiences rapid crack development along the pore spaces during the impact process, leading to partial pore penetration. This causes small pores to expand into larger ones, increasing the porosity. The crushed specimen transitions from large blocks to smaller ones, and the fractal dimension gradually decreases. When the strain rate exceeds  $64.67 s^{-1}$ , the specimen absorbs a large amount of energy instantaneously, preventing the cracks from expanding in time and leading to dense compression. The large pores are compressed and transformed into smaller pores, causing a reduction in porosity. The fragmentation of the specimen gradually becomes more homogeneous with smaller pieces, and the fractal dimension increases.

The 150–15,000 nm mesopores are subcritical defects in the material and are prone to serve as the core region for crack initiation and propagation under dynamic loading. As the strain rate increases, the speed of stress wave propagation accelerates, activating more mesopores as crack initiation points. This promotes the bifurcation of the primary crack into multiple secondary cracks, leading to a denser crack network that disperses the energy input, ultimately resulting in finer and more homogeneous fragments. When the strain rate exceeds a critical value ( $64.67 s^{-1}$ ), stress wave compression causes some macropores ( $>15,000$  nm) to collapse into mesopores. This compressive damage mode significantly reduces the fragment size, in line with the correlation between fragment size and strain rate described by the Grady-Kipp fragmentation theory. The increase in the proportion of mesopores suggests a more homogeneous distribution of defects within the material. As a result,

energy is dissipated through multiple paths under dynamic loading, reducing the dominance of a single main crack and making the material approach homogeneous damage.

## Conclusion

1. A well-defined critical strain rate for the dynamic mechanical response of cement-cured soils with Pisha Sandstone geopolymer is identified at  $64.67 \text{ s}^{-1}$ , which is significantly higher than the critical strain rate of conventional cementitious materials. When the strain rate is below this value, the coefficient of power increase shows a linear growth relationship with the logarithm of the strain rate. When the strain rate is between  $64.67$  and  $160 \text{ s}^{-1}$ , the coefficient continues to grow linearly with the logarithm of the strain rate but tends toward saturation.
2. Under impact loading, the porosity of the specimens after damage is significantly correlated with the strain rate. When the strain rate is lower than  $64.67 \text{ s}^{-1}$ , the proportion of small pores (10–150 nm) decreases, while the proportion of large pores (> 15,000 nm) increases with rising strain rate, with porosity being exponentially related to strain rate. When the strain rate exceeds  $64.67 \text{ s}^{-1}$ , the large pores collapse into medium pores (150–15,000 nm), causing the porosity to decrease, with a power function relationship to the strain rate.
3. The crushing characteristics of cement-cured soil with Pisha Sandstone geopolymer are significantly correlated with strain rate. The average block diameter decreases from 36.34 mm to 5.46 mm in a power function with increasing strain rate. The fractal dimension reaches a minimum at the critical strain rate, reflecting the most inhomogeneous distribution of fragments. Above the critical value, the fractal dimension gradually increases, indicating that the fragmentation process tends to become more homogeneous.
4. Combining macro-mechanical properties, pore structure changes, and multi-scale analysis of crushing characteristics, it is observed that when the strain rate is below  $64.67 \text{ s}^{-1}$ , pore-guided tensile damage dominates, while at strain rates above  $64.67 \text{ s}^{-1}$ , compression damage due to crowding becomes dominant. These findings provide a theoretical basis for dynamic proportioning design and damage warning of transportation infrastructure, such as roadbeds and protective structures, and offer a new perspective on studying the strain rate effect in porous brittle materials.

## Data availability

Data is provided within the manuscript information files.

Received: 29 September 2024; Accepted: 29 May 2025

Published online: 04 June 2025

## References

1. Liang, Z. et al. Pisha sandstone: Causes, processes and erosion options for its control and prospects. *Int. Soil. Water Conserv. Res.* **7**, 1–8. <https://doi.org/10.1016/j.iswcr.2018.11.001> (2019).
2. Feng, Z., Li, X., Shao, X. & Wang, L. Preferred injection method and curing mechanism analysis for the curing of loose Pisha sandstone based on microbially induced calcite precipitation. *Environ. Sci. Pollut. Res.* **30**, 12005–12019. <https://doi.org/10.1007/s11356-022-22742-1> (2022).
3. Zhang, P., Xiao, P., Yao, W., Liu, G. & Sun, W. Characteristics of sediment particle size distribution in the Pisha sandstone area of the middle yellow river under the effects of vegetation and complex erosion. *Earth Surf. Process. Land.* **48**, 1281–1289. <https://doi.org/10.1002/esp.5549> (2023).
4. Zhang, P., Li, L., Wang, J., Zhang, S. & Zhu, Z. Effects of hydraulic erosion on the Spatial redistribution characteristics of soil aggregates and SOC on Pisha sandstone slope. *Sustainability* **15**, 13276. <https://doi.org/10.3390/s1513276> (2023).
5. Geng, K., Chai, J., Qin, Y., Li, X. & Zhou, H. Collapse Inhibition mechanism analysis and durability properties of cement-stabilized Pisha sandstone. *Bull. Eng. Geol. Environ.* **81**, 1–8. <https://doi.org/10.1007/s10064-022-02642-x> (2022).
6. Zhao, J. et al. Eco-friendly geopolymer materials: A review of performance improvement, potential application and sustainability assessment. *J. Clean. Prod.* **307**, 127085. <https://doi.org/10.1016/j.jclepro.2021.127085> (2021).
7. Gu, L. et al. Effect of sodium silicate on the properties of loess stabilized with alkali-activated fly ash-based. *Constr. Build. Mater.* **280**, 122515. <https://doi.org/10.1016/j.conbuildmat.2021.122515> (2021).
8. Wang, S., Gao, X., Ma, W., Zhao, K. & Xu, P. Experimental study on static and dynamic characteristics of geopolymer-stabilized coarse-grained soils. *Acta Geotech.* **19**, 717–739. <https://doi.org/10.1007/s11440-023-01876-7> (2023).
9. Zhao, X., Li, X. & Li, D. Analysis of material changes in Pisha sandstone geopolymer composite cement-cured soil under dry-wet-salt intrusion coupling based on TG/DTA-FTIR. *Arch. Civ. Mech. Eng.* **25**, 142. <https://doi.org/10.1007/s43452-025-01202-w> (2025).
10. Ijaz, N., Ye, W., Rehman, Z. & Ijaz, Z. Novel application of low carbon limestone calcined clay cement (LC3) in expansive soil stabilization: An eco-efficient approach. *J. Clean. Prod.* **371**, 133492. <https://doi.org/10.1016/j.jclepro.2022.133492> (2022).
11. Wang, J., Fan, Y., Xiong, X. & Zhao, F. Stabilization of shield muck treated with calcium carbide slag-fly Ash. *Buildings* **13**, 1707. <https://doi.org/10.3390/buildings13071707> (2023).
12. Xiao, Y., Tong, L., Che, H., Guo, Q. & Pan, H. Experimental studies on compressive and tensile strength of cement-stabilized soil reinforced with rice husks and polypropylene fibers. *Constr. Build. Mater.* **344**, 128242. <https://doi.org/10.1016/j.conbuildmat.2022.128242> (2022).
13. Gong, X., Niu, J., Liang, S., Feng, D. & Luo, Q. Solidification of Nansha soft clay using cement-based composite curing agents. *Adv. Cem. Res.* **32**, 66–77. <https://doi.org/10.1680/jadcr.18.00040> (2020).
14. Sagidullina, N., Abdalim, S., Kim, J., Satyanaga, A. & Moon, S. W. Influence of freeze-thaw cycles on physical and mechanical properties of cement-treated silty sand. *Sustainability* **14**, 7000. <https://doi.org/10.3390/su14127000> (2022).
15. Yu, K., Deng, Y., Jiang, S. & Qiu, C. Strength and microscopic characteristics of slag-based geopolymer-solidified sludge after dry-wet cycling with chloride salt solutions. *Adv. Civ. Eng.* **2023**, 1–15. <https://doi.org/10.1155/2023/6691653> (2023).
16. Liu, K. et al. Effects of suffusion-induced contact variation on dynamic responses of saturated roadbed considering hydro-mechanical coupling under high-speed train loading. *Comput. Geotech.* **113**, 103095. <https://doi.org/10.1016/j.compgeo.2019.103095> (2019).
17. Dong, J., Wu, Z., Li, Z. & Yang, Y. Impact of cement-soil pile driven in railway subgrade horizontally on ground vibration. *Arab. J. Geosci.* **14**, 13. <https://doi.org/10.1007/s12517-021-06841-w> (2021).

18. Fan, H., Yu, H. & Ma, H. Dynamic increase factor (DIF) of concrete with SHPB tests: review and systematic analysis. *J. Build. Eng.* **79**, 107666. <https://doi.org/10.1016/j.job.2023.107666> (2023).
19. Wang, H. C., Zhao, J., Li, J., Braithwaite, C. H. & Zhang, Q. B. Progressive fracturing of concrete under biaxial confinement and repetitive dynamic loadings: from damage to catastrophic failure. *Int. J. Impact Eng.* **165**, 104232. <https://doi.org/10.1016/j.ijimpeng.2022.104232> (2022).
20. Ning, J., Meng, F., Ma, T., Xu, X. & Cheng, Z. Failure analysis of reinforced concrete slab under impact loading using a novel numerical method. *Int. J. Impact Eng.* **144**, 103647. <https://doi.org/10.1016/j.ijimpeng.2020.103647> (2020).
21. Pereira, L. F., Weerheijm, J. & Sluys, L. J. Simulation of compaction and crushing of concrete in ballistic impact with a new damage model. *Int. J. Impact Eng.* **111**, 208–221. <https://doi.org/10.1016/j.ijimpeng.2017.09.014> (2018).
22. Pan, J., Zhong, W., Wang, J. & Zhang, C. Size effect on dynamic splitting tensile strength of concrete: Mesoscale modeling. *Cem. Concr. Compos.* **128**, 104435. <https://doi.org/10.1016/j.cemconcomp.2022.104435> (2022).
23. Fu, J. et al. Investigating rock-breaking mechanisms under TBM hobs: Energy analysis and finite element modeling. *Strength. Mater.* **56**, 568–585. <https://doi.org/10.1007/s11223-024-00672-2> (2024).
24. Yang, Y. et al. Numerical investigation of stress and strain analysis in rock breaking of TBM disk cutters. *Strength. Mater.* **56**, 209–221. <https://doi.org/10.1007/s11223-024-00640-w> (2024).
25. Wang, L. et al. Numerical investigation on fracture propagation mechanism of pre-existing symmetrical cracks emanating from the circular blast holes. *Strength. Mater.* **55**, 1209–1214. <https://doi.org/10.1007/s11223-024-00611-1> (2023).
26. Sun, L. et al. Investigating the effect of various fibers on plasticity and compressive strength of concrete samples. *Strength. Mater.* **56**, 200–208. <https://doi.org/10.1007/s11223-024-00639-3> (2024).
27. Haeri, H. & Sarfarazi, V. The deformable multilaminate for predicting the elasto-plastic behavior of rocks. *Comput. Concret.* **18**, 201–214. <https://doi.org/10.12989/cac.2016.18.2.201> (2016).
28. Haeri, H. et al. Investigation of shear behavior of soil-concrete interface. *Smart Struct. Syst.* **23**, 81–90. <https://doi.org/10.12989/ss.2019.23.1.081> (2019).
29. Grady, D. E. & Kipp, M. E. Continuum modelling of explosive fracture in oil shale. *Int. J. Rock. Mech. Min. Sci. Geomech. Abstr.* **17**, 147–157. [https://doi.org/10.1016/0148-9062\(80\)91361-3](https://doi.org/10.1016/0148-9062(80)91361-3) (1980).
30. Zhao, H. Material behaviour characterisation using SHPB techniques, tests and simulations. *Comput. Struct.* **81**, 1301–1310. [https://doi.org/10.1016/s0045-7949\(03\)00044-0](https://doi.org/10.1016/s0045-7949(03)00044-0) (2003).
31. Xu, D., Zhang, Z., Qin, Y., Liu, T. & Cheng, Z. Effect of particle size distribution on dynamic properties of cemented coral sand under SHPB impact loading. *Soil. Dyn. Earthq. Eng.* **162**, 107438. <https://doi.org/10.1016/j.soildyn.2022.107438> (2022).
32. Huang, R., Guan, Z., Qin, J., Wen, Y. & Lai, Z. Strain rate effect of concrete based on split Hopkinson pressure bar (SHPB) test. *J. Build. Eng.* **86**, 108856. <https://doi.org/10.1016/j.job.2024.108856> (2024).
33. Ren, L., Yu, X., Guo, Z. & Xiao, L. Numerical investigation of the dynamic increase factor of ultra-high performance concrete based on SHPB technology. *Constr. Build. Mater.* **325**, 126756. <https://doi.org/10.1016/j.conbuildmat.2022.126756> (2022).
34. Zhang, J. & Zhang, J. Experimental study and analysis of the static and dynamic mechanical properties of graphene oxide cement soil under composite salinity erosion. *Constr. Build. Mater.* **451**, 138848. <https://doi.org/10.1016/j.conbuildmat.2024.138848> (2024).
35. Feng, S., Yu, Y. & Liu, Y. Experimental study on the dynamic mechanical properties and failure characteristics of in situ cemented backfill under impact loading. *Min. Metall. Explor.* **2025**, 1–11. <https://doi.org/10.1007/s42461-025-01268-3> (2025).
36. Zhao, Z. et al. Experimental research on the dynamic constraining characteristics and fractal properties of sandstone under impact loading. *Case Stud. Constr. Mater.* **18**, e02174. <https://doi.org/10.1016/j.cscm.2023.e02174> (2023).
37. Michel, S. & Sipos, A. A. Fragmentation of inflated elastic brittle rings: Emergence of the quasi-equidistant spacing of cracks. *J. Mech. Phys. Solids.* **179**, 105372. <https://doi.org/10.1016/j.jmps.2023.105372> (2023).

## Acknowledgements

The authors gratefully acknowledge the financial supports provided by the National Natural Science Foundation of China (42467042). Inner Mongolia Autonomous Region Postgraduate Research Innovation Program(K-C2024045B).

## Author contributions

Author Xiaoze Zhao's contribution to the article was mainly original draft writing, data management. Author Xiaoli Li's contribution to the article was mainly funding acquisition, review and editing. Author Zhuojun Feng's contribution to the article was mainly verification, supervision.

## Declarations

### Competing interests

The authors declare no competing interests.

### Additional information

**Correspondence** and requests for materials should be addressed to X.L.

**Reprints and permissions information** is available at [www.nature.com/reprints](http://www.nature.com/reprints).

**Publisher's note** Springer Nature remains neutral with regard to jurisdictional claims in published maps and institutional affiliations.

**Open Access** This article is licensed under a Creative Commons Attribution-NonCommercial-NoDerivatives 4.0 International License, which permits any non-commercial use, sharing, distribution and reproduction in any medium or format, as long as you give appropriate credit to the original author(s) and the source, provide a link to the Creative Commons licence, and indicate if you modified the licensed material. You do not have permission under this licence to share adapted material derived from this article or parts of it. The images or other third party material in this article are included in the article's Creative Commons licence, unless indicated otherwise in a credit line to the material. If material is not included in the article's Creative Commons licence and your intended use is not permitted by statutory regulation or exceeds the permitted use, you will need to obtain permission directly from the copyright holder. To view a copy of this licence, visit <http://creativecommons.org/licenses/by-nc-nd/4.0/>.

© The Author(s) 2025